The impact of nanostructure on hygroscopicity and reactivity of fatty acid atmospheric aerosol proxies

Adam Milsom,[1] Adam M. Squires,[2] Ben Laurence,[2] Ben Woden,[3] Andrew J. Smith,[4] Andrew D. Ward[5] and Christian Pfrang.[1,6,*]

[1]School of Geography, Earth and Environmental Sciences, University of Birmingham, Edgbaston, B15 2TT, Birmingham, UK.

[2]Department of Chemistry, University of Bath, South Building, Soldier Down Ln, Claverton Down, BA2 7AX, Bath, UK.

[3]Department of Chemistry, University of Reading, RG6 6AD, Reading, Berkshire, UK

[4]Diamond Light Source, Diamond House, Harwell Science and Innovation Campus, OX11 0DE, Didcot, UK.

[5]Central Laser Facility, STFC Rutherford Appleton Laboratory, Didcot OX11 0FA, UK

[6]Department of Meteorology, University of Reading, Whiteknights, Earley Gate, RG6 6BB, Reading, UK.

*Corresponding author: Professor Christian Pfrang (c.pfrang@bham.ac.uk)

Abstract

Atmospheric aerosol hygroscopicity and reactivity play key roles in determining the aerosol's fate and are strongly affected by its composition and physical properties. Fatty acids are surfactants commonly found in organic aerosol emissions. They form a wide range of different nanostructures dependent on water content and mixture composition. In this study we follow nano-structural changes in mixtures frequently found in urban organic aerosol emissions, i.e. oleic acid, sodium oleate and fructose, during humidity change and exposure to the atmospheric oxidant ozone. Addition of fructose altered the nanostructure by inducing molecular arrangements with increased surfactant-water interface curvature. Small-Angle X-ray Scattering (SAXS) was employed for the first time to derive the hygroscopicity of each nanostructure by measuring time- and humidity-resolved changes in nano-structural parameters. We found that hygroscopicity is directly linked to the specific nanostructure and is dependent on the nanostructure geometry. Reaction with ozone revealed a clear nanostructure-reactivity trend, with notable differences between the individual nanostructures investigated. Simultaneous Raman microscopy complementing the SAXS studies revealed the persistence of oleic acid even after extensive oxidation. Our findings demonstrate that self-assembly of fatty acid nanostructures can significantly impact two key atmospheric aerosol processes: water uptake and chemical reactivity, thus directly affecting the atmospheric lifetime of these materials. This could have significant impacts on both urban air quality (e.g. protecting harmful urban emissions from atmospheric degradation and therefore enabling their long-range transport), and climate (e.g. affecting cloud formation), with implications for human health and wellbeing.

Introduction

Atmospheric aerosols represent a large uncertainty when considering their impact on the climate (Boucher et al., 2013; Shrivastava et al., 2017) and urban particulate matter makes a

significant contribution to air pollution, affecting air quality and health (Shrivastava et al., 2017;
Harrison, 2020; Chan and Yao, 2008; Pöschl, 2005). Organic matter can account for a large
portion of aerosol emissions depending on the emission source (Jimenez et al., 2009) and
environmental conditions have been shown to affect aerosol composition (Li et al., 2021).
There are both anthropogenic and biogenic sources of organic aerosols. Activities such as
cooking emit a range of organic compounds which can go on to form secondary organic
aerosol (SOA) (Zeng et al., 2020). Cooking emissions have been estimated to add *ca*. 10 %
to UK $PM_{2.5}$ emissions (Ots et al., 2016) and have been linked with poor air quality (Stavroulas
et al., 2023).

Oleic acid is a fatty acid and a common organic compound found in both cooking (Zeng et al.,
2020; Alves et al., 2020; Vincente et al., 2018) and marine emissions (Fu et al., 2013). It is
reactive towards common atmospheric oxidants such as ozone and NO_3, making it a model
compound for laboratory studies into aerosol properties (Zahardis and Petrucci, 2007;
Gallimore et al., 2017; Pfrang et al., 2017; Pfrang et al., 2011; Pfrang et al., 2010; King et al.,
2010; Sebastiani et al., 2022; Shiraiwa et al., 2012; Shiraiwa et al., 2010). Other common
organic emissions are saccharides (sugars), which are also found in urban (Wang et al., 2006)
and biogenic emissions (Fu et al., 2013; Fu et al., 2008; Kirpes et al., 2019). Sugar emissions
such as levoglucosan and glucose have been shown to react readily with Criegee
intermediates, which are formed during ozonolysis (Enami et al., 2017). The fact that these
two common classes of organic compounds (fatty acids and sugars) are found in the same
aerosol samples raises the possibility that they are able to interact; for example by a sugar
reacting with oleic acid ozonolysis Criegee intermediates, potentially altering the product
distribution and adding to the complexity of this reaction mechanism – a possibility explored
in this study.

Aerosol phase state has been predicted to vary significantly in the atmosphere and is linked
to factors such as composition, humidity and temperature (Shiraiwa et al., 2017; Schmedding
et al., 2020). One key influence on aerosol multiphase processes is particle viscosity (Reid et
al., 2018) and viscous phases have been identified by field measurements of SOA (Virtanen
et al., 2010). Particle viscosity can vary by orders of magnitude between phase states, which
means the diffusion coefficients of small molecules through the particle phase also vary and
heterogeneous processes (*i.e.* oxidation and water uptake) are affected (Shiraiwa et al., 2011;
Koop et al., 2011). Viscous phases can induce diffusion gradients during particle
humidification (Zobrist et al., 2011; Hosny et al., 2016; Renbaum-Wolff et al., 2013). Particles
of oleic acid have also been observed to increase in viscosity as a result of oxidation (Hosny
et al., 2016). The fate of organic atmospheric aerosols is therefore strongly influenced by their
phase state.

Organic coatings are present on the surface of marine aerosols, where sugars and fatty acids
were found to be major constituents (Kirpes et al., 2019). Poor air quality has been linked to
high $PM_{2.5}$ surface organic content in Beijing, China (Zhao et al., 2020) and the long-range
transport of harmful substances emitted in the urban environment have been attributed to
viscous organic coatings and the phase state of the aerosol (Shrivastava et al., 2017; Mu et
al., 2018). Analysis of marine aerosols heavily influenced by anthropogenic activity found that
fatty acids were present along with Polycyclic Aromatic Hydrocarbons (PAHs) and phthalates,
which are known to cause poor health (Kang et al., 2017). There is a long-standing
discrepancy between the longer lifetime measured in the field compared to laboratory
measurements for oleic acid (Rudich et al., 2007; Wang and Yu, 2021). These observations
suggest that aerosols are able to travel far from their sources and that the formation of viscous
organic coatings could account for their long-range transport.

Pure oleic acid in the liquid phase exhibits some order by the formation of dimers (Iwahashi et
al., 1991). As a surfactant, the addition of its ionic form (sodium oleate) and water can induce
the formation of lyotropic liquid crystal (LLC) phases (Tiddy, 1980). These are three-
dimensional nanostructures which can vary from spherical and cylindrical micelles to
bicontinuous networks and lamellar sheets. These structures can be followed by Small-Angle
X-ray Scattering (SAXS), which probes the nanometre scale. Each of these structures exhibit
varying physical properties, the key ones being diffusivity and viscosity. Diffusion coefficients
can vary dramatically between micellar, close-packed micellar, hexagonal (cylindrical micellar)
and lamellar phases with diffusion in the latter two becoming directionally dependent
(Lindblom and Orädd, 1994; Orädd et al., 1995). The diffusion of atmospherically relevant
small molecules, such as ozone and water, would therefore also be affected by the
nanostructure formed in the organic medium, affecting the key aerosol heterogeneous
processes of water uptake and chemical reaction.

We have previously demonstrated the feasibility of LLC formation in levitated particles of a
fatty acid aerosol proxy (Pfrang et al., 2017; Milsom et al., 2023; Milsom et al., 2022a) and
have exploited the SAXS experiment to quantify the effect of self-assembly on reaction kinetics
(Milsom et al., 2021a), along with modelling of the potential impact on the atmospheric lifetime
of LLC formation (Milsom et al., 2022b). In this study we coat capillaries with a self-assembled
oleic acid/sodium oleate/fructose proxy use SAXS to follow changes in these nanostructures
during humidity cycles and exposure to ozone. We investigate the sensitivity of the
nanostructure to proxy composition and humidity and demonstrate that reactivity is affected
by nanostructure.

Methods

Preparation of self-assembled coatings inside quartz capillaries

The method of film preparation is identical to that described in Milsom et al. (2021a) Sample
coating solutions were prepared as follows: oleic acid (Sigma-Aldrich, 90 %), sodium oleate
(Sigma-Aldrich, 99 %) and fructose (Sigma-Aldrich, 99 %) were dissolved as 10 wt % solutions
in methanol and samples weighed to the desired ratio. All coating solutions are weighed as
1:1:x wt ratio mixtures (oleic acid:sodium oleate:fructose), where x is 0.5, 1, 2 corresponding
to 20, 33 and 50 wt % fructose compositions.

**SAXS experiment and simultaneous Raman microscopy on films coated inside quartz
capillaries**

SAXS probes aggregates at the nanometre scale, measuring order at the molecular, rather
than atomic (X-ray diffraction), scale (Li et al., 2016; Pauw, 2013). The scattered intensity is
measured against a scattering parameter (q) which is proportional to the scattering angle. q is
inversely proportional to the characteristic spacing between equivalent scattering planes (d)
via equation 1. This is also a measure of the spacings between inverse micelles.

$$d = \frac{2\pi}{q} \text{ (1)}$$

This d-spacing can be used to determine a range of nano-structural parameters - for example,
the water layer thickness between lamellar sheets (Kulkarni et al., 2011; Milsom et al., 2022c).

This experimental setup is the same as used in our previous capillary film study (Milsom et al.,
2021a). Key experimental parameters are listed here: SAXS patterns were collected as 1s
exposures at different positions along the coated capillary with a delay of 75 s between each

scan to avoid any X-ray beam damage; the beam size at the sample was approximately 320 x 400 μm (FWHM); SAXS patterns were acquired between q = 0.008 – 0.6 Å^{-1} by a *Pilatus P3-2M* detector.

The Raman microscopy setup is as described in Milsom et al. (2021a): A 532-nm Raman laser probe was focussed with a long working distance objective (numerical aperture: 0.42) and a minimum spot diameter of ~ 1.5 μm. The emitted laser power was 20 – 50 mW. By following the oleic acid C=C bond peak at ~ 1650 cm^{-1} and normalising to the –CH$_2$ peak at ~ 1442 cm^{-1}, we were able to follow the progress of the ozonolysis reaction simultaneous to the SAXS measurements.

Ozonolysis of coated films

The ozonolysis procedure follows what was set out previously (Milsom et al., 2021a) and is summarised here: Oxygen (BOC, 99.5 %) was passed through a pen-ray ozoniser (Ultraviolet Products Ltd., Cambridge, UK) which was calibrated offline by UV spectroscopy; the ozone concentration for all ozonolysis experiments was 77 ± 5 ppm at a flow rate of 60 mL min^{-1}. Note that such a high ozone concentration (typical atmospheric concentrations are ppb level) was used as it is known that self-assembled semi-solid phases slow the rate of reaction significantly (Pfrang et al., 2017; Milsom et al., 2021a). The ozone-oxygen mixture was measured to be at < 5 % RH.

Film thickness was determined by X-ray beam attenuation using diodes measuring the incident and transmitted intensities. The maximum attenuation was determined by filling a capillary with sample material. The thickness of each coated film was then calibrated by comparison with the filled capillary's attenuation.

Controlled humidification of coated films

Humidity was monitored and controlled using a bespoke Raspberry Pi (RPi) system. Dry (room air) and wet pumps were controlled by the RPi, in order to reach the target relative humidity (RH), which was measured by a sensor at the outlet of the coated capillary tube with a precision of 2 %.

After samples were coated, they were left for ~ 15 min to equilibrate at room humidity (~ 50 – 60 % RH) before being attached to the humidity control system. The capillary was then humidified to the desired settings using the RPi control programme.

Results and Discussion

176   **Time- and humidity-resolved nanostructure changes**
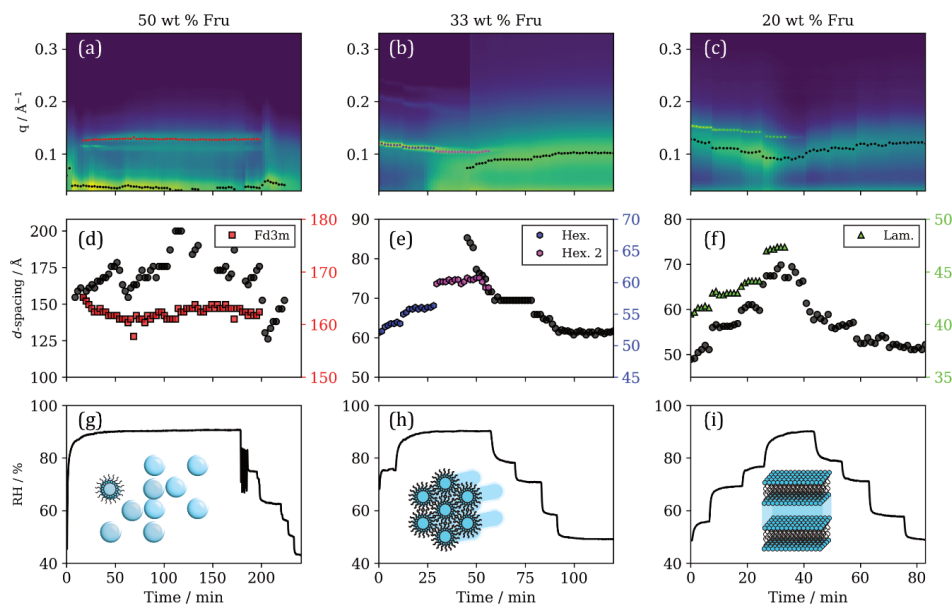
178   Figure 1. (a)-(c) SAXS patterns as a function of time during the humidity cycle. Peak positions
       for inverse micellar (black markers) and specific nanostructures (coloured markers) are q
180   values corresponding to the time-resolved d-spacings represented in (d)-(f). (g)-(i)
       Simultaneous RH vs time during the experiment. Each set of SAXS, d-spacing and RH data
182   is presented for each proxy fructose composition as wt % of organic mass with oleic acid and
       sodium oleate in a 1:1 wt ratio: (a), (d), (g) – 50 wt %; (b), (e), (h) – 33 wt %; (c), (f), (i) – 20 wt
184   % (*i.e.* 50 wt % fructose is a 1:1:2 oleic acid:sodium oleate:fructose mixture).

       Different amounts of fructose in the organic mixture result in different self-assembled
186   nanostructures (Fig. 1(a)-(c)). From first principles fructose, as a hydrophilic water-soluble
       molecule, would be expected to facilitate water uptake into the organic phase and act as a
188   humectant, analogous to the effect glycerol has on LLC phase boundaries (Richardson et al.,
       2015). By this logic, larger amounts of fructose should afford more hydrated (lower water-
190   surfactant interfacial curvature) phases at a given humidity. However, an additional effect is
       observed during our experiments: the water-surfactant interfacial curvature *increases* with
192   increasing fructose concentration. This is clear evidence for fructose acting as a *kosmotrope*
       – a water-structure-inducing molecule (Kulkarni et al., 2011; Libster et al., 2008; Koynova et
194   al., 1997). As a kosmotrope, fructose removes water from the water-surfactant interface. This
       reduces the effective surfactant headgroup area, enabling the formation of structures with
196   increased curvature at a given water content (in this case, experimental humidity – see
       corresponding cartoons of each phase in Fig. 1). The phase boundary therefore shifts
198   according to the amount of fructose in the mixture. A set of fructose content-dependent
       nanostructures are possible as a result. Each one of these nanostructures possesses unique
200   physical properties (as set out in the introduction). The sensitivity of the nanostructure to the
       amount of fructose in the system suggests that the physical properties, which influence

202   atmospheric trace gas uptake, could also change with similar sensitivity to aerosol composition.

204   The characteristic *d*-spacing for each of the observed nanostructures increases with increasing RH (Fig 1. (d)-(f)). This is the result of water filing the aqueous cavity in the inverse
206   LLC nanostructures observed here. The time and humidity-resolved SAXS patterns acquired in this study have allowed us to take advantage of this characteristic and observe subtle RH-
208   dependent changes in this parameter and directly measure the water uptake of a specific phase. This analysis can be applied to two coexistent phases, provided their SAXS peaks do
210   not overlap – as is the case in our study. The effect of these phases on water uptake is explored in *Hygroscopicity of observed nanostructures*.

212   The phase change observed when going from low to high RH is not reversible for the two organic compositions which initially formed inverse hexagonal and lamellar phases at < 90 %
214   RH (Fig. 1(b) and (c)). This suggests that the initial or final phases observed are meta-stable (e.g. the Fd3m and P6$_3$/mmc inverse micellar cubic phases can occur under the same
216   conditions for this system; Pfrang et al., 2017). Fig. 1(d–f) shows that for a given phase equilibrated with water vapour at a particular RH, the *d*-spacing is stable. This suggests that
218   these phases are in equilibrium, even if they are meta-stable.

      For the 33 wt % fructose mixture, a second hexagonal phase appears at high RH before
220   eventually transitioning to an inverse micellar phase (Fig. 1(b) and (e)). Indeed, between ~ 40 – 60 min the inverse micellar and hexagonal phase are observed simultaneously in the
222   mixture. There therefore is a heterogeneity in terms of molecular order and physical properties associated with each of these nanostructures. This coexistent inverse micellar phase is
224   observed for all mixtures studied here.

      The 50 wt % fructose mixture exhibits a reversible phase transition from inverse micellar to a
226   close-packed inverse micellar (Fd3m) phase during a humidification-dehumidification cycle (Fig. 1(a)). The Fd3m phase appeared only at the highest humidity setting (90 % RH). The
228   phase transition does not involve a significant change in phase topology, making the transition more facile compared with the transition to a hexagonal or lamellar phase - although the Fd3m
230   arrangement is thought to include inverse micelles of differing size (Seddon et al., 1990; Shearman et al., 2010).

232
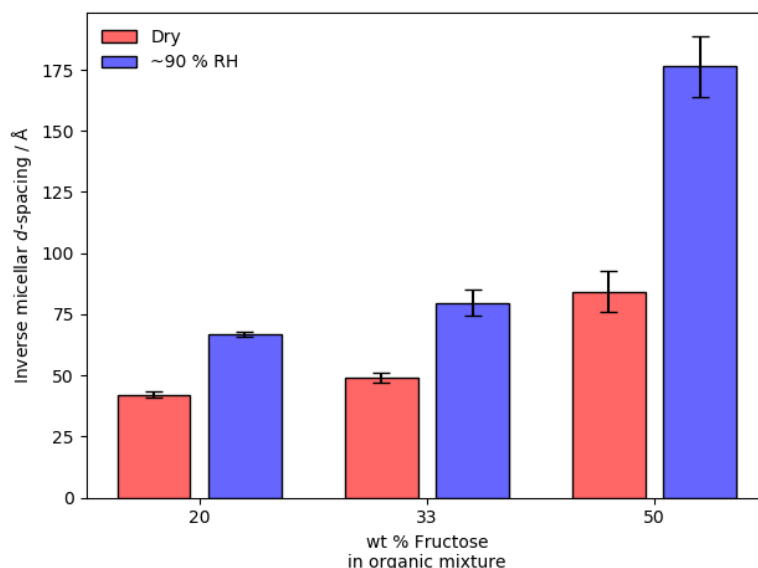
Figure 2. Inverse micellar *d*-spacing vs wt % fructose in the organic mixture under dry (~ 5 %
234 RH) and humid (~ 90 % RH) conditions. A clear increase in *d*-spacing is visible upon
humidification of each organic film.

236 A coexistent inverse micellar phase is observed for all organic compositions during these
humidity experiments (Fig. 1(a)-(c) – broad peak at lower *q* values). This coexistence
238 represents a heterogeneity within the organic film, implying a similar heterogeneity in physical
properties. We cannot say for certain whether this phase separation is uniform throughout the
240 film using this technique. However, the visible shift in the inverse micellar peak position during
humidity changes suggests that the change is happening in the majority of the film *i.e.* the
242 inverse micellar is distributed throughout the film.

The inverse micellar *d*-spacing increases with the amount of fructose in the mixture under dry
244 and humid conditions (Fig. 2). The inverse micellar phase observed for all fructose-containing
mixtures studied here has a much larger *d*-spacing than mixtures without fructose, where a *d*-
246 spacing of ~28-32 Å is expected (Fig. S1 – SAXS of a hydrated levitated particle of this
composition; Mele et al., 2018). Fructose therefore stabilises larger inverse micelles. Notably,
248 under dry (~5 % RH) conditions fructose seems to have a marked effect on the inverse micellar
d-spacing. This implies that fructose is collecting within the inverse micellar core and that
250 possibly some water has been accommodated within the structure, explaining the increase in
the average repeat distance between inverse micelles.

252 Increasing the humidity substantially increases the inverse micellar *d*-spacing for all
compositions. This effect is most potent for the 50 wt % fructose mixture (Fig. 2). The
254 observation highlights the ability of fructose to act as a humectant and stabilise large inverse
micelles. It is worth restating that these inverse micellar phases at high RH are coexistent with
256 more ordered phases. A measure of the hygroscopicity for each coexistent phase can be
extracted from the SAXS data and is presented in *Hygroscopicity of observed nanostructures*.

258

Hygroscopicity of observed nanostructures

260   We have compared the hygroscopicity of the observed phases with what can be calculated
from Raoult's law for fructose over the RH range studied here.
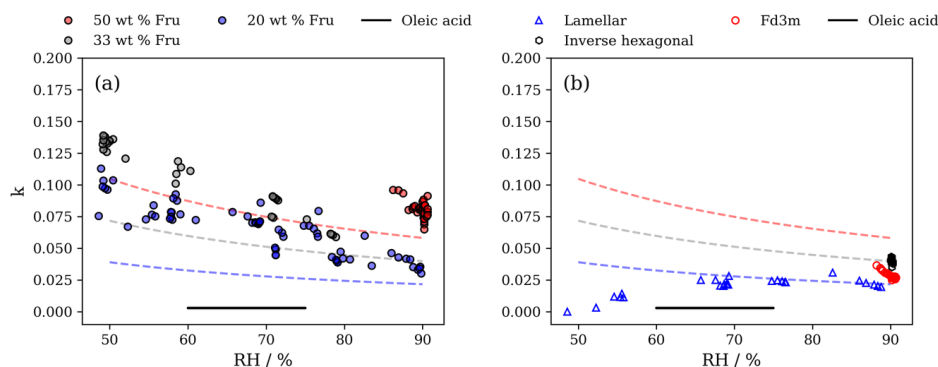
262   Figure 3. Plots of hygroscopicity parameter (κ) derived from d-spacings vs RH for the inverse
micellar phases at different weight percentage fructose (wt % Fru) (a) and for other
264   nanostructures including the lamellar phase (at 20 wt % fructose), inverse hexagonal (at 33
wt % fructose) and close-packed inverse micellar (Fd3m, at 50 wt % fructose) (b). Dashed
266   lines on both plots represent κ calculated for the same fructose-lipid ratio based on Raoult's
law at a particular RH. The colours of the dashed lines correspond to the wt % fructose in the
268   mixture. The κ value for oleic acid measured by Rickards et al. (2013) is also plotted for
reference (κ = 0.003 ± 0.001).

270   κ-Köhler theory derives aerosol hygroscopicity from particle sizes at different water activities
(a_w; Petters and Kreidenweis, 2007). The characteristic d-spacing calculated for each
272   nanostructure observed here is related to its water content. We have applied κ-Köhler theory
by measuring the change in d-spacing with a_w, to describe the hygroscopicity of each phase.
274   RH was converted to a_w (a_w = RH/100) and it is assumed that the proxy film had equilibrated
with the humidity inside the capillary (see the rapid change and equilibration of the d-spacing
276   observed when changing RH in Fig. 1). Note that κ-Köhler theory is normally applied to aerosol
particles linking particle growth with humidity. Here we are not measuring individual particles,
278   we are measuring nanoscale changes in the structural repeat distances, which are correlated
with water content. Equation 2 links the dry (V_d) and water (V_w) volumes with a_w and a
280   hygroscopicity parameter (κ; Petters and Kreidenweis, 2007).

$$\frac{V_w}{V_d} = \frac{a_w}{(1-a_w)}\kappa \quad (2)$$

282   The calculation of κ is based on the geometry of each phase and the information regarding
the mass and volume fractions of the lipid and water regions derivable from the equilibrium d-
284   spacings obtained by SAXS (Asghar et al., 2015; Kulkarni et al., 2011). A detailed explanation
of the calculation of κ is provided in the ESI.

286   This parameterisation of hygroscopicity is based on a simplified model which does not account
for non-ideal solution behaviour. Also, these experiments are not carried out on particle
288   ensembles or single particles, as has been the application previously (Liu et al., 2021;
Rickards, 2013). As theories of hygroscopicity are in general agreement at higher a_w (RH)
290   (Rickards, 2013; Clegg et al., 1998; Wexler and Clegg, 2002; Fredenslund et al., 1975;
Topping et al., 2005; Zuend et al., 2008; Zuend et al., 2011), our measurements of κ at high

RH (maximum 90 % RH) are the most informative. However, we caution the over-interpretation of these κ values in the context of other hygroscopicity studies due to the experimental differences between this study and others. These κ measurements do however provide a first insight into the hygroscopic behaviour of these nanostructures and comparison between these results is justified by the same method used to calculate κ.

The disordered inverse micellar phase formed at each composition is higher than what is predicted by Raoult's law for fructose (Fig. 3(a)). These predictions assume that it is only the fructose that takes up water. Therefore, the formation of the inverse micellar nanostructure, in addition to the hygroscopicity of the fructose, increases κ beyond what would be expected from the hygroscopicity of fructose alone.

The close-packed inverse micellar phase (Fd3m symmetry) appears to be less hygroscopic than the Raoult prediction by a factor of ~ 2 at 90 % RH (Fig. 3(b)). This is in contrast to the disordered inverse micelles coexistent with this nanostructure (Fig. 3(a)). The key difference between the two nanostructures is that the close-packed inverse micelles are restricted in space. The inverse hexagonal and lamellar phases are in better agreement with Raoult's law predictions at > 85 % RH (Fig. 3(b)).

The lamellar phase appears to become much less hygroscopic at low RH. This may be because of an increase in the inter-bilayer attractive forces at lower bilayer separations and/or more restricted alkyl chains resulting from a more crystalline bilayer (Bahadur et al., 2019). A crystalline form of this lamellar bilayer has been observed in similar systems (Tandon et al., 2001; Milsom et al., 2021b).

As a thermodynamic parameter, κ reflects the energy changes involved in changing the nano-structural parameters associated with phase hydration and dehydration. For the lamellar phase, work must be done in order to overcome inter- and intra-bilayer repulsion when increasing and decreasing the volume of water between bilayers (Parsegian et al., 1979). To clarify, if there is attraction between bilayers, then it is easier for the lamellar phase to lose water (i.e. lower κ at lower humidities where there is less distance and greater attraction between bilayers). In the inverse hexagonal phase, the elastic free energy change associated with a change in cylindrical radius is related to a bending modulus and the curvature of the cylinder, both of which are associated with the bilayer-forming lipid and are affected by the addition of other interacting molecules (Chen and Rand, 1997). The close-packed inverse micellar phase is more sterically restricted than the disordered inverse micelles. The disordered inverse micellar phase has the least frustrated hydrocarbon tails out of the nanostructures presented here (*i.e.* they are not constrained close together, as is the case in the hexagonal and lamellar phases). Removing water from inverse micelles requires more energy to do because of the increased curvature that results, explaining the increased κ values for inverse micelles compared with the lamellar, inverse hexagonal and inverse cubic close-packed phases under similar conditions. These nanostructure-specific considerations help explain the difference between experiment and prediction.

All κ values derived from our SAXS data are greater than what has been measured for pure oleic acid (Fig. 3; Rickards et al., 2013). The addition of fructose alone does not account for all of the differences in κ observed between pure oleic acid, predictions based on Raoult's law and the nanostructured fatty acid proxy. There must be an effect of the nanostructure formed and this effect is most pronounced for the disordered inverse micellar phase.

336   **Reactivity-nanostructure relationship**
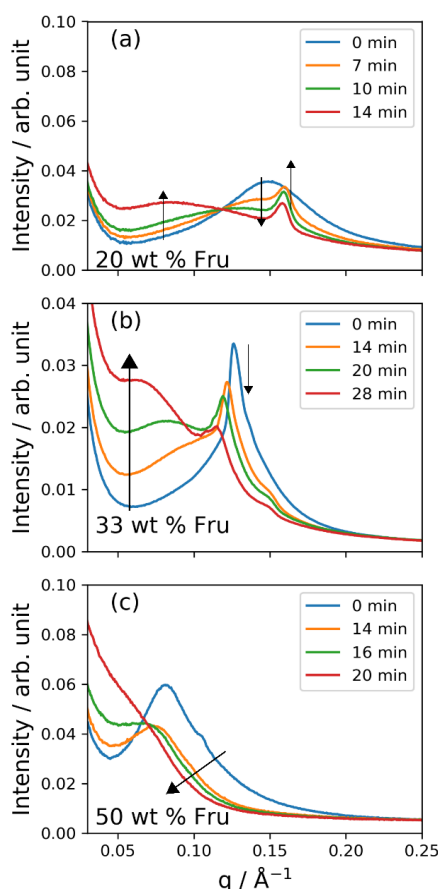
338   Figure 4. 1D SAXS patterns during ozonolysis of mixtures of: (a) 20 wt % fructose, (b) 33 wt
        % fructose and (c) 50 wt % fructose. Note the shift to low-q of the broad inverse micellar peak
340   for each composition. An additional phase appears in the first few minutes of reaction for the
        20 wt % fructose mixture (a). The additional peaks associated with the ordered inverse micellar
342   ($P6_3/mmc$) are revealed after ~ 20 min for the 33 wt % fructose mixture (b) – these are indexed
        in the ESI. [O_3] = 77 ± 5 ppm, RH < 5 %.

344   We subjected proxy coatings of fatty acid-fructose mixtures to ozonolysis under dry conditions
        analogous to our previous film kinetic study (Milsom et al., 2021a). Figure 4 presents the SAXS
346   patterns and phases observed during ozonolysis for the fructose-containing mixtures studied
        here. There are broad peaks characteristic of the inverse micellar phase in all mixtures, this
348   was the most commonly observed phase under these conditions. An extra feature from an
        ordered phase appears during ozonolysis for the 20 wt % fructose mixture (Fig. 4(a)) – this is
350   discussed in conjunction with simultaneous Raman spectrometry later (see Fig. 6). An ordered
        phase is observed for the 33 wt % fructose film (Fig. 4(b)). Initially, the less intense peaks
352   associated with this phase are obscured by the broad overlapping inverse micellar peak. After
        ~ 20 min of ozonolysis the broad peak has shifted to lower q and the other peaks are visible.

354 These peaks index closest to an ordered micellar phase with P6$_3$/mmc symmetry, which has
been observed before in levitated droplets of a similar proxy (Pfrang et al., 2017) – see ESI
356 for phase indexing. This allowed us to measure the kinetic difference between ordered and
disordered inverse micelles.

358
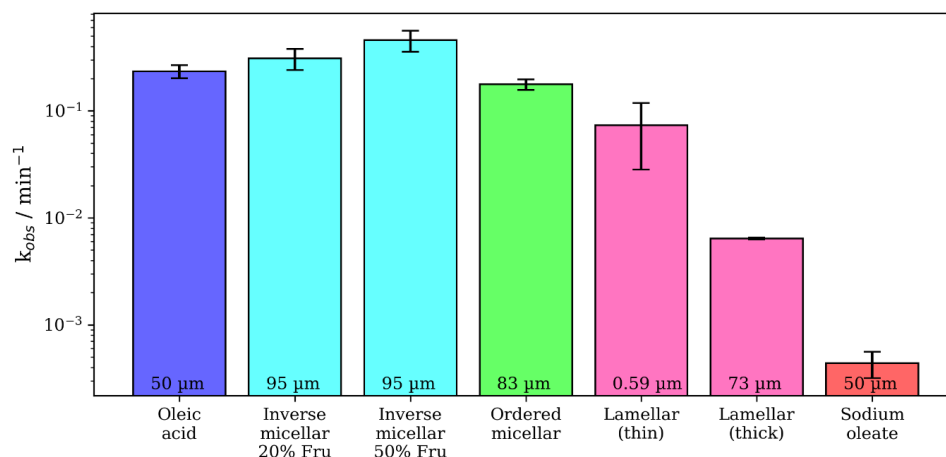
360 Figure 5. Pseudo-first order decay constants (k_{obs}) measured for the oleic acid-ozone reaction
carried out on coated films of different composition and nanostructure. The thickness of each
362 film is displayed at the bottom of each bar (see Table S1 in the ESI for all kinetic data and
associated uncertainties). Oleic acid, sodium oleate and lamellar phase data are taken from
364 earlier work (Milsom et al., 2021a). The lamellar phase was formed in a dry mixture of oleic
acid: sodium oleate (1:1 wt). Oleic acid and sodium oleate decays were measured by following
366 the C=C peak in the Raman spectrum as described in the methods. [O$_3$] = 77 ± 5 ppm and RH
< 5 %.

368 Reaction kinetics can be followed by SAXS using an analysis technique that we have
developed (Milsom et al., 2021a). We took advantage of the time resolution offered by a
370 synchrotron experiment to derive kinetic parameters for coated organic films of different
composition and nanostructure (Fig. 5). All kinetic data are summarised in Table S1 and a
372 more detailed derivation of these kinetic decay parameters is presented in Milsom et al.
(2021a).

374 The disordered inverse micellar phase reacts faster than the ordered micellar phase coated
at a similar thickness. This is to be expected as the close-packed inverse micelles are locked
376 into their position, increasing the viscosity of the phase and therefore slowing the diffusion of
small molecules such as ozone. The viscosity of close-packed inverse micelles can be in the
378 order of 10^4 times higher than for the disordered inverse micelles (Pouzot et al., 2007).

An order of reactivity exists between nanostructures. We are now able to compare the
380 reactivity of different phases formed by this proxy system and the reactivity of its constituent
parts (Fig. 5). Going from most to least reactive: inverse micellar > close-packed inverse
382 micellar > (dry) lamellar. Note that the lamellar phase in this case is anhydrous. As suggested
by Hearn *et al.*, diffusion of ozone past the closely packed lamellar chains is likely to be
384 hindered and the rate of reaction reduced as a result, limiting the reaction to the surface of the
film (Hearn et al., 2005).

386 The close-packed (ordered) inverse micellar phase film was ~ 12 μm thinner than the inverse
micellar films. We have shown previously that film thickness can affect reactivity (Milsom et
388 al., 2021a),[44] so we cannot rule out the effect of film thickness in these experiments. Though
it was not possible to control film thickness, comparisons are still possible and actually reveal
390 some stark differences in reactivity. Most notably is the comparison of the sub-micron lamellar
phase film with ~ 95 μm films of inverse micellar phase. The thin lamellar phase film reacts
392 slower than the inverse micellar films despite the ~ 160-fold difference in film thicknesses.
There is also a difference of nearly two orders of magnitude between the thickest lamellar film
394 (73 μm) and the inverse micellar films (95 μm).
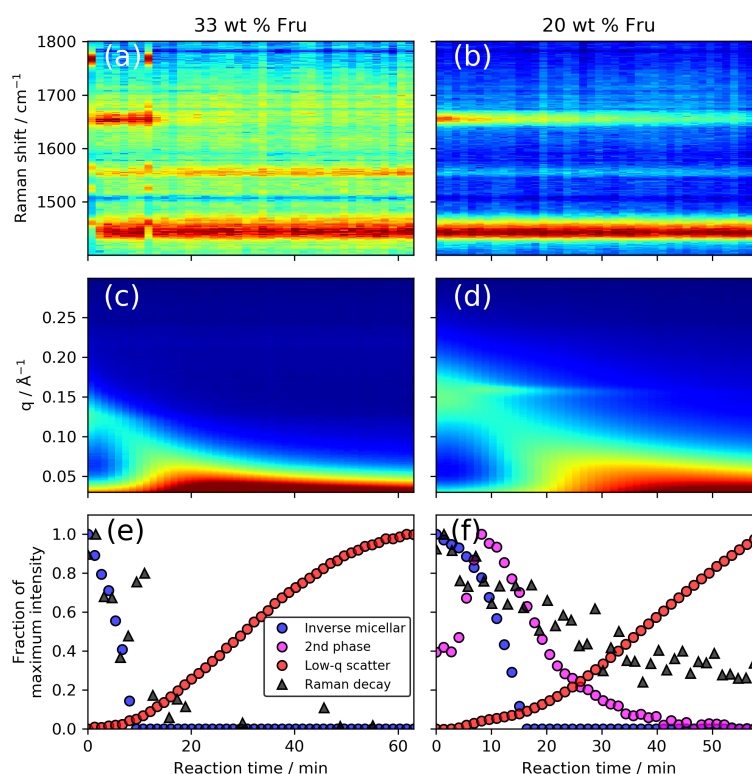
Figure 6. (a) and (b) Raman spectra vs reaction time highlighting the disappearance of the
396 oleic acid C=C peak at ~ 1650 cm^{-1} and the persistence of the –CH$_2$ deformation band at ~
1442 cm^{-1} for the 33 and 20 wt % fructose compositions, respectively. (c) and (d) simultaneous
398 SAXS patterns vs reaction time showing the initial broad inverse micellar peak (0.12-0.15 Å^{-1})
which shifts to lower q and disappears. The increase in low-q scattering is also evident along
400 with the appearance of a 2nd phase peak for the 20 wt % fructose composition (d). (e) and (f)
Plots of maximum peak area intensity vs reaction time for key SAXS and Raman peaks.
402 Raman decay is measured by following the C=C/-CH$_2$ peak area ratio.

The inverse micellar d-spacing increases (q decreases) as ozonolysis progresses (Fig. 6).
404 This experiment was carried out under dry conditions, so the increase in spacing must be a
result of the reaction rather than any water uptake. We suggest that fructose itself reacts with
406 one of the intermediate products. Common saccharides found in the atmosphere, including
glucose (closely related to fructose), have been shown to react readily with Criegee
408 intermediates that are formed as a result of ozonolysis (Enami et al., 2017). This forms ethers

of greater mass and therefore products are likely to take up more space, accounting for the increase in *d*-spacing observed during our ozonolysis experiment. Fructose can form an ether with oleic acid, however, to the author's knowledge, this has only been observed as an enzymatic reaction (Ye and Hayes, 2011). Reaction with a Criegee intermediate is therefore the most probable explanation.

Products may themselves self-assemble. The increase in low-*q* scattering observed here was not observed during reactions of similar samples without fructose (Milsom et al., 2021a). This suggests that the species causing the increased low-*q* scatter is associated with the fructose in the system. If high-molecular-weight fructose products are formed, the marked increase in low-*q* scatter suggests that these molecules aggregate into structures with large repeat distances.

A new phase was formed in the with a peak in *q*-range of *ca.* 0.14–0.16 Å during the ozonolysis of the 20 wt % fructose mixture (Fig. 4(a) and Fig. 6(d)). This was unexpected as it was assumed that self-assembly would be destroyed by chemical reaction of the constituent fatty acid, as observed previously (Pfrang et al., 2017; Milsom et al., 2021a). This phase took longer to disappear compared with the initial inverse micellar phase. The reaction induced heterogeneity in the film both in the nanostructure and corresponding physical properties. This observation suggests that there is a dynamic relationship between nanostructure and the chemical reaction of this fatty acid aerosol proxy. The identity of this phase is uncertain due to the lack of a 2nd order peak in the SAXS pattern, however this peak appears where the dry lamellar phase peak is expected to occur (Milsom et al., 2021a; Mele et al., 2018) – this is the most likely arrangement. The atmospheric implications of the effect of nanostructure on reaction kinetics will be discussed in the following section.

There is evidence that the oleic acid double-bond persists at the end of the reaction (Fig. 6(b)). Simultaneous Raman spectroscopy on our deposited films shows clearly that the carbon-carbon double-bond peak associated with oleic acid is still present at the end of the reaction even though the initial SAXS peaks are not visible. The increase in inverse micellar *d*-spacing (SAXS peak shift to lower *q*), the notable increase in low-*q* scattering and the persistence of the double-bond suggests that oleic acid may be protected by the increase in viscosity expected by the formation of larger molecular mass molecules, which have been identified as products for the oleic acid-ozone system (Reynolds et al., 2006; Zahardis et al., 2005). This persistence is consistent with recent work on coated capillaries and residues observed after oxidising monolayers of atmospheric surfactants (including oleic acid) coated on water (Milsom et al., 2021a; Woden et al., 2021; Woden et al., 2018; Sebastiani et al., 2022; Sebastiani et al., 2018; King et al., 2009; Pfrang et al., 2014). This highlights the utility of a simultaneous technique to measure reaction kinetics (Raman spectroscopy).

Atmospheric implications

A wide distribution of aerosol phase states in the atmosphere has been observed and predicted with global chemistry models (Shiraiwa et al., 2017; Schmedding et al., 2020; Virtanen et al., 2010). This phase state is dependent on the aerosol's environment, which includes humidity and temperature. Aerosol multiphase processes are strongly affected by the formation of semi-solid and glassy phases due to reduced gas-particle interactions and the effect on particle diffusivity (Berkemeier et al., 2016; Zhou et al. 2019; Zhou et al. 2013; Mikhailov et al., 2009: Koop et al., 2011; Zobrist et al., 2011). This in turn leads to phase-dependent increases in aerosol atmospheric lifetimes, and can facilitate the long-range transport of an aerosol substantially. Particle phase state and viscous aerosol organic coatings

10.5194/egusphere-2024-905
2024-04-05
EGUsphere
journal article
en

456 have been linked to the long-range transport of polycyclic aromatic hydrocarbons (PAHs), which are particularly harmful to human health by acting as carcinogens (Shrivastava et al.,
458 2017; Mu et al., 2018).

In the work presented here, we are adding a further organic aerosol component to our bottom-
460 up approach for this fatty acid aerosol proxy system with the addition of the sugar fructose, which is commonly found in urban emissions. The addition of fructose induces nano-structural
462 changes by acting as a kosmotrope under humidified conditions. This shows that the nanostructure depends on the organic composition in addition to the relative humidity. In this
464 study, we quantify two key properties affected by the nanostructure: hygroscopicity and reactivity.

466 As illustrated in Fig. 3, the nanostructure increases the hygroscopicity parameter (κ) by as much as a factor of ca. 10 to 50 compared to liquid oleic acid. Hygroscopicity determines the
468 water uptake of aerosol at a specific RH; we have previously shown (Milsom et al., 2022a) that aerosol water content strongly impacts on viscosity.

470 Fig. 5 shows that the aerosol reactivity changes by nearly two orders of magnitude when altering the nano-structural arrangement e.g. between a 73-µm thick lamellar film and a 95-
472 µm thick inverse micellar film. This strong effect of nanostructure on aerosol reactivity is likely due to changes in viscosity and diffusivity.

474 Previously, we have shown that ozonolysis destroys self-assembly in fatty acid aerosol proxies (Pfrang et al., 2017; Milsom et al., 2021a). Here we additionally show that ozonolysis can
476 induce the formation of a new intermediate molecular arrangement (see Fig. 6(d)), demonstrating the possibility that self-assembly could be induced by the chemical reaction of
478 these atmospheric molecules with ozone. This, in combination with humidity-induced phase changes, suggests a dynamic aerosol phase state which is dependent on the molecular
480 arrangement of the surfactant molecules.

Atmospheric aerosols exhibit heterogeneity both in terms of composition and physical
482 properties (Kirpes et al., 2019; Schill et al., 2015). Particle viscosity can become heterogeneous during chemical reaction and exposure to humidity (Hosny et al., 2016). We
484 have now demonstrated that nano-structural heterogeneity exists during humidity change and ozonolysis where different nanostructures coexist. There must therefore be a heterogeneity in
486 hygroscopicity in our proxy films due to the link between nanostructure and κ (see Fig. 3). The formation of an intermediate nanostructure during ozonolysis observed here suggests that
488 viscosity may not be equal throughout the film and that the diffusivity of small molecules such as ozone throughout the particle would also not be uniform, affecting the lifetime of the proxy
490 (Shiraiwa et al, 2011b). The increase in d-spacing we observed between inverse micelles during ozonolysis suggests that larger molecules are formed as a result of the reaction (see
492 Fig. 4 and Fig. 6(c) & (d)). These larger molecules may also contribute to film heterogeneity and alter the reactive lifetime of these molecules.

494 Sugars and fatty acids, such as fructose and oleic acid, are commonly encountered components of aerosols emitted in urban (Wang et al., 2006) and marine (Fu et al., 2013)
496 environments. Specifically, saccharides (sugars) have been identified along with fatty acids as major components of thick (µm-scale) organic coatings observed on sea spray aerosols
498 (Kirpes et al., 2019) and also in a cafeteria environment (Alves et al., 2020), demonstrating the wide range of environments our proxies represent. Their relative abundances can vary
500 significantly depending on season, time of day and location. In this study we have shown that the proxy sugar content has a substantial impact on aerosol physical properties via a change
502 in nanostructure. We conclude that, as the relative amount of sugar and fatty acid changes

504 between environments, nanostructures could also vary depending on the location and emission type.

506 We have now demonstrated that the reactivity of surface-active oleic acid depends not only on whether it is self-assembled (Pfrang et al., 2017; Milsom et al., 2021a), but also on the specific nanostructure it adopts (see Fig. 5). Our results suggest that the lifetime of surfactant

508 material would depend on nanostructure, which in turn is linked to aerosol composition. The persistence of surface-active material has been demonstrated at the air-water interface

510 (Woden et al., 2021; Woden et al., 2018; Sebastiani et al., 2022; Sebastiani et al., 2018; King et al., 2009; Pfrang et al., 2014). Simultaneous Raman microscopy suggests that oleic acid

512 can persist in the films studied here, a finding consistent with non-fructose-containing films of this proxy (Milsom et al., 2021a). We have demonstrated that the reactive lifetime of oleic acid

514 can vary by orders of magnitude as a result of different molecular arrangements. There is a link between surfactant content and cloud droplet formation potential as a result of a reduction

516 in surface tension (Bzdek et al., 2020; Ovadnevaite et al., 2017; Facchini et al., 2000; Facchini et al., 1999). Therefore, any increase in surfactant lifetime would imply a similar increase of

518 the cloud formation potential of a surfactant-containing aerosol, such as aerosols emitted from cooking or sea spray containing oleic acid and/or related species.

520

Conclusions

522 Our work has clearly shown that changes in the nanostructure, induced by humidity changes, can directly affect both water uptake and reactivity which are known to be two key aerosol

524 ageing processes.[e.g. Pöschl, 2005]

Crucially, we have demonstrated and quantified the direct link between the nanostructures

526 formed by fructose-containing fatty acid mixtures and the key aerosol properties of hygroscopicity and reactivity for the first time by utilising synchrotron SAXS and complimentary

528 Raman microscopy. This combination of SAXS and Raman data allowed us to infer key atmospheric aerosol properties and extract information from coexistent nanostructures to draw

530 comparisons between these. As a result, heterogeneity could be revealed during humidity exposure and ozonolysis. Our findings demonstrate that self-assembly of fatty acid

532 nanostructures can massively alter both water uptake and chemical reactivity, with significant impacts on (i) urban air quality by protecting harmful urban emissions from atmospheric

534 degradation and therefore enabling their long-range transport; and (ii) climate by affecting cloud formation. This could have fundamental implications for human health and wellbeing.

536

Data access statement

538 Data supporting with this study are available in the supporting information and from the corresponding author upon request.

540

Conflicts of interest

542 There are no conflicts to declare.

544

Acknowledgements

546   This work was carried out with the support of the Diamond Light Source (DLS), instrument I22 (proposal SM21663). AM wishes to acknowledge funding from NERC SCENARIO DTP award

548   number NE/L002566/1 and CENTA DTP. The work was supported by NERC (research grant NE/T00732X/1). The authors would like to thank Nick Terrill (DLS), Tim Snow (DLS) and Lee

550   Davidson (DLS) for technical support during beamtime experiments; Jacob Boswell is acknowledged for help at beamtimes. The authors are grateful to the Central Laser Facility for

552   access to key equipment for the Raman work simultaneously to the DLS beamtime experiments.

554

References

556   Alves, C. A., E. D. Vicente, M. Evtyugina, A. M. Vicente, T. Nunes, F. Lucarelli, G. Calzolai, S. Nava, A. I. Calvo, C. del B. Alegre, F. Oduber, A. Castro and R. Fraile, *Atmos.*

558   *Pollut. Res.*, 2020, **11**, 531–544.

Asghar, K. A., D. A. Rowlands, J. M. Elliott and A. M. Squires, *ACS Nano*, 2015, **9**, 10970–

560   10978.

Bahadur, J., A. Das and D. Sen, *J. Appl. Crystallogr.*, 2019, **52**, 1169–1175.

562   Berkemeier, T., S. S. Steimer, U. K. Krieger, T. Peter, U. Pöschl, M. Ammann and M. Shiraiwa, *Phys. Chem. Chem. Phys.*, 2016, **18**, 12662–12674.

564   Boucher, O., D. Randall, P. Artaxo, C. Bretherton, G. Feingold, P. Forster, V.-M. Kerminen, Y. Kondo, H. Liao, U. Lohmann, P. Rasch, S. K. Satheesh, S. Sherwood, B. Stevens

566   and X. Y. Zhang, in *Climate Change 2013 - The Physical Science Basis*, ed. Intergovernmental Panel on Climate Change, Cambridge University Press,

568   Cambridge, 2013, pp. 571–658.

Bzdek, B. R., J. P. Reid, J. Malila and N. L. Prisle, *Proc. Natl. Acad. Sci. U. S. A.*, 2020, **117**,

570   8335–8343.

Chan, C. K. and X. Yao, *Atmos. Environ.*, 2008, **42**, 1–42.

572   Chen, Z. and R. P. Rand, *Biophys. J.*, 1997, **73**, 267–276.

Clegg, S. L., P. Brimblecombe and A. S. Wexler, *J. Phys. Chem. A*, 1998, **102**, 2155–2171.

574   Enami, S., M. R. Hoffmann and A. J. Colussi, *J. Phys. Chem. Lett.*, 2017, **8**, 3888–3894.

Facchini, M. C., S. Decesari, M. Mircea, S. Fuzzi and G. Loglio, *Atmos. Environ.*, 2000, **34**,

576   4853–4857.

Facchini, M. C., M. Mircea, S. Fuzzi and R. J. Charlson, *Nature*, 1999, **401**, 257–259.

578   Fredenslund, A., R. L. Jones and J. M. Prausnitz, *AIChE J.*, 1975, **21**, 1086–1099.

Fu, P. Q., K. Kawamura, J. Chen, B. Charrière and R. Sempéré, *Biogeosciences*, 2013, **10**,

580   653–667.

Fu, P., K. Kawamura, K. Okuzawa, S. G. Aggarwal, G. Wang, Y. Kanaya and Z. Wang, *J.*

582   *Geophys. Res. Atmos.*, 2008, **113**, 1–20.

Gallimore, P. J., P. T. Griffiths, F. D. Pope, J. P. Reid and M. Kalberer, *J. Geophys. Res.*,

584   2017, **122**, 4364–4377.

Harrison, R. M. *Philos. Trans. R. Soc. A Math. Phys. Eng. Sci.*, 2020, **378**, 20190319.

586 Hearn, J. D., G. D. Smith and A. J. Lovett, *Phys. Chem. Chem. Phys.*, 2005, **7**, 501–511.

Hosny, N. A., C. Fitzgerald, A. Vyšniauskas, A. Athanasiadis, T. Berkemeier, N. Uygur, U.
588 Pöschl, M. Shiraiwa, M. Kalberer, F. D. Pope and M. K. Kuimova, *Chem. Sci.*, 2016,
7, 1357–1367.

590 Iwahashi, M., Y. Yamaguchi, T. Kato, T. Horiuchi, I. Sakurai and M. Suzuki, *J. Phys. Chem.*,
1991, **95**, 445–451.

592 Jimenez, J. L., M. R. Canagaratna, N. M. Donahue, A. S. H. Prevot, Q. Zhang, J. H. Kroll, P.
F. DeCarlo, J. D. Allan, H. Coe, N. L. Ng, A. C. Aiken, K. S. Docherty, I. M. Ulbrich, A.
594 P. Grieshop, A. L. Robinson, J. Duplissy, J. D. Smith, K. R. Wilson, V. A. Lanz, C.
Hueglin, Y. L. Sun, J. Tian, A. Laaksonen, T. Raatikainen, J. Rautiainen, P.
596 Vaattovaara, M. Ehn, M. Kulmala, J. M. Tomlinson, D. R. Collins, M. J. Cubison, J.
Dunlea, J. A. Huffman, T. B. Onasch, M. R. Alfarra, P. I. Williams, K. Bower, Y.
598 Kondo, J. Schneider, F. Drewnick, S. Borrmann, S. Weimer, K. Demerjian, D.
Salcedo, L. Cottrell, R. Griffin, A. Takami, T. Miyoshi, S. Hatakeyama, A. Shimono, J.
600 Y. Sun, Y. M. Zhang, K. Dzepina, J. R. Kimmel, D. Sueper, J. T. Jayne, S. C.
Herndon, A. M. Trimborn, L. R. Williams, E. C. Wood, A. M. Middlebrook, C. E. Kolb,
602 U. Baltensperger and D. R. Worsnop, *Science (80-.).*, 2009, **326**, 1525–1529.

Kang, M., F. Yang, H. Ren, W. Zhao, Y. Zhao, L. Li, Y. Yan, Y. Zhang, S. Lai, Y. Zhang, Y.
604 Yang, Z. Wang, Y. Sun and P. Fu, *Sci. Total Environ.*, 2017, **607**–**608**, 339–350.

King, M. D., A. R. Rennie, C. Pfrang, A. V. Hughes and K. C. Thompson, *Atmos. Environ.*,
606 2010, **44**, 1822–1825.

King, M. D., A. R. Rennie, K. C. Thompson, F. N. Fisher, C. C. Dong, R. K. Thomas, C.
608 Pfrang and A. V. Hughes, *Phys. Chem. Chem. Phys.*, 2009, **11**, 7699–7707.

Kirpes, R. M., D. Bonanno, N. W. May, M. Fraund, A. J. Barget, R. C. Moffet, A. P. Ault and
610 K. A. Pratt, *ACS Cent. Sci.*, 2019, **5**, 1760–1767.

Koop, T., J. Bookhold, M. Shiraiwa and U. Pöschl, *Phys. Chem. Chem. Phys.*, 2011, **13**,
612 19238–19255.

Koynova, R., J. Brankov and B. Tenchov, *Eur. Biophys. J.*, 1997, **25**, 261–274.

614 Kulkarni, C. V., W. Wachter, G. Iglesias-Salto, S. Engelskirchen and S. Ahualli, *Phys. Chem.
Chem. Phys.*, 2011, **13**, 3004–3021.

616 Li, G., H. Su, N. Ma, J. Tao, Y. Kuang, Q. Wang, J. Hong, Y. Zhang, U. Kuhn, S. Zhang, X.
Pan, N. Lu, M. Tang, G. Zheng, Z. Wang, Y. Gao, P. Cheng, W. Xu, G. Zhou, C.
618 Zhao, B. Yuan, M. Shao, A. Ding, Q. Zhang, P. Fu, Y. Sun, U. Pöschl and Y. Cheng,
Faraday Discuss., 2021, DOI:10.1039/D0FD00099J.

620 Li, T., A. J. Senesi and B. Lee, *Chem. Rev.*, 2016, **116**, 11128–11180.

Libster, D., P. Ben Ishai, A. Aserin, G. Shoham and N. Garti, *Langmuir*, 2008, **24**, 2118–
622 2127.

Lindblom, G. and G. Orädd, *Prog. Nucl. Magn. Reson. Spectrosc.*, 1994, **26**, 483–515.

624 Liu, J., F. Zhang, W. Xu, L. Chen, J. Ren, S. Jiang, Y. Sun and Z. Li, *J. Geophys. Res.
Atmos.*, 2021, **126**, 1–11.

626 Mele, S., O. Söderman, H. Ljusberg-Wahrén, K. Thuresson, M. Monduzzi and T. Nylander,
Chem. Phys. Lipids, 2018, **211**, 30–36.

628 Mikhailov, E., S. Vlasenko, S. T. Martin, T. Koop and U. Pöschl, *Atmos. Chem. Phys.*, 2009,
9, 9491–9522.

630   Milsom, A., A. M. Squires, A. D. Ward and C. Pfrang, *Acc. Chem. Res.*, 2023, **56**, 2555–
           2568.

632   Milsom, A., A. M. Squires, I. Quant, N. J. Terrill, S. Huband, B. Woden, E. R. Cabrera-
           Martinez and C. Pfrang, *J. Phys. Chem. A*, 2022a, **126**, 7331–7341.

634   Milsom, A., A. M. Squires, A. D. Ward and C. Pfrang, *Atmos. Chem. Phys.*, 2022b, **22**,
           4895–4907.

636   Milsom, A., A. M. Squires, M. W. A. Skoda, P. Gutfreund, E. Mason, N. J. Terrill and C.
           Pfrang, *Environ. Sci. Atmos.*, 2022c, **2**, 964–977.

638   Milsom, A., A. M. Squires, B. Woden, N. J. Terrill, A. D. Ward and C. Pfrang, *Faraday
           Discuss.*, 2021a, **226**, 364–381.

640   Milsom, A., A. M. Squires, J. A. Boswell, N. J. Terrill, A. D. Ward and C. Pfrang, *Atmos.
           Chem. Phys.*, 2021b, **21**, 15003–15021, doi.org/10.5194/acp-21-15003-2021.

642   Mu, Q., M. Shiraiwa, M. Octaviani, N. Ma, A. Ding, H. Su, G. Lammel, U. Pöschl and Y.
           Cheng, *Sci. Adv.*, 2018, **4**, eaap7314.

644   Orädd, G., G. Lindblom, K. Fontell and H. Ljusberg-Wahren, *Biophys. J.*, 1995, **68**, 1856–
           1863.

646   Ots, R., M. Vieno, J. D. Allan, S. Reis, E. Nemitz, D. E. Young, H. Coe, C. Di Marco, A.
           Detournay, I. A. Mackenzie, D. C. Green and M. R. Heal, *Atmos. Chem. Phys.*, 2016,
648   **16**, 13773–13789.

       Ovadnevaite, J., A. Zuend, A. Laaksonen, K. J. Sanchez, G. Roberts, D. Ceburnis, S.
650   Decesari, M. Rinaldi, N. Hodas, M. C. Facchini, J. H. Seinfeld and C. O'Dowd, *Nature*,
           2017, **546**, 637–641.

652   Parsegian, V. A., N. Fuller and R. P. Rand, *Proc. Natl. Acad. Sci. U. S. A.*, 1979, **76**, 2750–
           2754.

654   Pauw, B. R. *J. Phys. Condens. Matter*, 2013, **25**, 383201.

       Petters, M. D. and S. M. Kreidenweis, *Atmos. Chem. Phys.*, 2007, **7**, 1961–1971.

656   Pfrang, C., K. Rastogi, E. R. Cabrera-Martinez, A. M. Seddon, C. Dicko, A. Labrador, T. S.
           Plivelic, N. Cowieson and A. M. Squires, *Nat. Commun.*, 2017, **8**, 1724.

658   Pfrang, C., F. Sebastiani, C. O. M. Lucas, M. D. King, I. D. Hoare, D. Chang and R. A.
           Campbell, *Phys. Chem. Chem. Phys.*, 2014, **16**, 13220–13228.

660   Pfrang, C., M. Shiraiwa and U. Pöschl, *Atmos. Chem. Phys.*, 2011, **11**, 7343–7354.

       Pfrang, C., M. Shiraiwa and U. Pöschl, *Atmos. Chem. Phys.*, 2010, **10**, 4537–4557.

662   Pöschl, U. *Angew. Chemie Int. Ed.*, 2005, **44**, 7520–7540.

       Pouzot, M., R. Mezzenga, M. Leser, L. Sagalowicz, S. Guillote and O. Glatter, *Langmuir*,
664   2007, **23**, 9618–9628.

       Reid, J. P., A. K. Bertram, D. O. Topping, A. Laskin, S. T. Martin, M. D. Petters, F. D. Pope
666   and G. Rovelli, *Nat. Commun.*, 2018, **9**, 1–14.

       Renbaum-Wolff, L., J. W. Grayson, A. P. Bateman, M. Kuwata, M. Sellier, B. J. Murray, J. E.
668   Shilling, S. T. Martin and A. K. Bertram, *Proc. Natl. Acad. Sci.*, 2013, **110**, 8014–8019.

       Reynolds, J. C., D. J. Last, M. McGillen, A. Nijs, A. B. Horn, C. Percival, L. J. Carpenter and
670   A. C. Lewis, *Environ. Sci. Technol.*, 2006, **40**, 6674–6681.

Richardson, S. J., P. A. Staniec, G. E. Newby, J. L. Rawle, A. R. Slaughter, N. J. Terrill, J. M. Elliott and A. M. Squires, *Chem. Commun.*, 2015, **51**, 11386–11389.

Rickards, A. M. J., R. E. H. Miles, J. F. Davies, F. H. Marshall and J. P. Reid, *J. Phys. Chem. A*, 2013, **117**, 14120–14131.

Rudich, Y., N. M. Donahue and T. F. Mentel, *Annu. Rev. Phys. Chem.*, 2007, **58**, 321–352.

Schill, S. R., D. B. Collins, C. Lee, H. S. Morris, G. A. Novak, K. A. Prather, P. K. Quinn, C. M. Sultana, A. V. Tivanski, K. Zimmermann, C. D. Cappa and T. H. Bertram, *ACS Cent. Sci.*, 2015, **1**, 132–141.

Schmedding, R., Q. Z. Rasool, Y. Zhang, H. O. T. Pye, H. Zhang, Y. Chen, J. D. Surratt, F. D. Lopez-Hilfiker, J. A. Thornton, A. H. Goldstein and W. Vizuete, *Atmos. Chem. Phys.*, 2020, **20**, 8201–8225.

Sebastiani, F., R. A. Campbell and C. Pfrang, *Environ. Sci.: Atmos.*, 2022, **2**, 1324–1337.

Sebastiani, F., R. A. Campbell, K. Rastogi and C. Pfrang, *Atmos. Chem. Phys.*, 2018, **18**, 3249–3268.

Seddon, J. M., E. A. Bartle and J. Mingins, *J. Phys. Condens. Matter*, 1990, **2**, SA285–SA290.

Shearman, G. C., A. I. I. Tyler, N. J. Brooks, R. H. Templer, O. Ces, R. V. Law and J. M. Seddon, *Liq. Cryst.*, 2010, **37**, 679–694.

Shiraiwa, M., Y. Li, A. P. Tsimpidi, V. A. Karydis, T. Berkemeier, S. N. Pandis, J. Lelieveld, T. Koop and U. Pöschl, *Nat. Commun.*, 2017, **8**, 1–7.

Shiraiwa, M., C. Pfrang, T. Koop and U. Pöschl, *Atmos. Chem. Phys.*, 2012, **12**, 2777–2794.

Shiraiwa, M., M. Ammann, T. Koop and U. Poschl, *Proc. Natl. Acad. Sci. U. S. A.*, 2011a, **108**, 11003–11008.

Shiraiwa, M., M. Ammann, T. Koop and U. Pöschl, *Proc. Natl. Acad. Sci. USA*, 2011b, **108**, 11003-11008, Supplementary material: DOI:10.1073/pnas.1103045108/-/DCSupplemental.

Shiraiwa, M., C. Pfrang and U. Pöschl, *Atmos. Chem. Phys.*, 2010, **10**, 3673–3691.

Shrivastava, M., C. D. Cappa, J. Fan, A. H. Goldstein, A. B. Guenther, J. L. Jimenez, C. Kuang, A. Laskin, S. T. Martin, N. L. Ng, T. Petaja, J. R. Pierce, P. J. Rasch, P. Roldin, J. H. Seinfeld, J. Shilling, J. N. Smith, J. A. Thornton, R. Volkamer, J. Wang, D. R. Worsnop, R. A. Zaveri, A. Zelenyuk and Q. Zhang, *Rev. Geophys.*, 2017a, **55**, 509–559.

Shrivastava, M., S. Lou, A. Zelenyuk, R. C. Easter, R. A. Corley, B. D. Thrall, P. J. Rasch, J. D. Fast, S. L. M. Simonich, H. Shen and S. Tao, *Proc. Natl. Acad. Sci. U. S. A.*, 2017b, **114**, 1246–1251.

Stavroulas, I., A. Bougiatioti, G. Grivas, E. Liakakou, K. Petrinoli, K. Kourtidis, E. Gerasopoulos and N. Mihalopoulos, *Sci. Total Environ.*, 2023, DOI:10.1016/j.scitotenv.2023.168031.

Tandon, P., S. Raudenkolb, R. H. H. Neubert, W. Rettig and S. Wartewig, *Chem. Phys. Lipids*, 2001, **109**, 37–45.

Tiddy, G. J. T., *Phys. Rep.*, 1980, **57**, 1–46.

Topping, D. O., G. B. McFiggans and H. Coe, *Atmos. Chem. Phys.*, 2005, **5**, 1205–1222.

Vicente, E. D., A. Vicente, M. Evtyugina, R. Carvalho, L. A. C. Tarelho, F. I. Oduber and C. Alves, *Fuel Process. Technol.*, 2018, **176**, 296–306.

Virtanen, A., J. Joutsensaari, T. Koop, J. Kannosto, P. Yli-Pirilä, J. Leskinen, J. M. Mäkelä, J. K. Holopainen, U. Pöschl, M. Kulmala, D. R. Worsnop and A. Laaksonen, *Nature*, 2010, **467**, 824–827.

Wang, Q. and J. Z. Yu, *Geophys. Res. Lett.*, 2021, DOI:10.1029/2021GL095130.

Wang, G., K. Kawamura, L. Shuncheng, K. Ho and J. Cao, *Environ. Sci. Technol.*, 2006, **40**, 4619–4625.

Wexler, A. S. and S. L. Clegg, *J. Geophys. Res.*, 2002, **107**, 4207.

Woden, B., M. W. A. Skoda, A. Milsom, C. Gubb, A. Maestro, J. Tellam and C. Pfrang, *Atmos. Chem. Phys.*, 2021, **21**, 1325–1340.

Woden, B., M. Skoda, M. Hagreen and C. Pfrang, *Atmosphere (Basel)*, 2018, **9**, 471.

Ye, R. and D. G. Hayes, *JAOCS, J. Am. Oil Chem. Soc.*, 2011, **88**, 1351–1359.

Zahardis, J. and G. A. Petrucci, *Atmos. Chem. Phys.*, 2007, **7**, 1237–1274.

Zahardis, J., B. W. LaFranchi and G. A. Petrucci, *J. Geophys. Res. D Atmos.*, 2005, **110**, 1–10.

Zeng, J., Z. Yu, M. Mekic, J. Liu, S. Li, G. Loisel, W. Gao, A. Gandolfo, Z. Zhou, X. Wang, H. Herrmann, S. Gligorovski and X. Li, *Environ. Sci. Technol. Lett.*, 2020, **7**, 76–81.

Zhao, Y., H. Huang, Y. Zhang, K. Wu, F. Zeng, J. Wang, X. Yu, Z. Zhu, X.-Y. Yu and F. Wang, *Atmos. Environ.*, 2020, **220**, 117090.

Zhou, S., B. C. H. Hwang, P. S. J. Lakey, A. Zuend, J. P. D. Abbatt and M. Shiraiwa, *Proc. Natl. Acad. Sci. U. S. A.*, 2019, **116**, 11658–11663.

Zhou, S., M. Shiraiwa, R. D. McWhinney, U. Pöschl and J. P. D. Abbatt, *Faraday Discuss.*, 2013, **165**, 391–406.

Zobrist, B., V. Soonsin, B. P. Luo, U. K. Krieger, C. Marcolli, T. Peter and T. Koop, *Phys. Chem. Chem. Phys.*, 2011, **13**, 3514–3526.

Zuend, A., C. Marcolli, A. M. Booth, D. M. Lienhard, V. Soonsin, U. K. Krieger, D. O. Topping, G. McFiggans, T. Peter and J. H. Seinfeld, *Atmos. Chem. Phys.*, 2011, **11**, 9155–9206.

Zuend, A., C. Marcolli, B. P. Luo and T. Peter, *Atmos. Chem. Phys.*, 2008, **8**, 4559–4593.

714

716

718

720

722

724

726

728

730

732

734

736

738

740

742